This manuscript is a preprint and has been submitted for publication in *Geophysical Journal International.* Please note that the manuscript is undergoing peer review and has not been accepted for publication. Subsequent versions of this manuscript may have slightly different content. If accepted, the final version of this manuscript will be available via the 'Peer-reviewed Publication DOI' link on the right-hand side of this webpage. Please feel free to contact the corresponding author; we welcome feedback.

Within the subducting Nazca Plate: The 2020 Mw 6.8 Calama earthquake and its similarity with the surrounding inslab seismicity

Carlos Herrera[1,2], Francisco Pastén-Araya[3,4], Leoncio Cabrera[5], Bertrand Potin[3], Efraín Rivera[4], Sergio Ruiz[3], Raúl Madariaga[3], Eduardo Contreras-Reyes[3]

[1] School of Earth and Ocean Sciences, University of Victoria, Victoria, BC, Canada

[2] Now at: Onur Seemann Consulting, Inc., Victoria, BC, Canada

[3] Departamento de Geofísica, Facultad de Ciencias Físicas y Matemáticas, Universidad de Chile, Santiago, Chile

[4] Departamento de Obras Civiles, Facultad de Ciencias de la Ingeniería, Universidad Católica del Maule, Talca, Chile

[5] ISTerre Institut des Sciences de la Terre, CNRS, Université Grenoble Alpes, Grenoble, France

Corresponding author: Carlos Herrera (carlos@onurseemann.com)

Abbreviated title: "The Calama inslab earthquake"

Summary

We study the 2020 M_W 6.8 Calama earthquake sequence that occurred within the subducting oceanic Nazca plate. The mainshock is modeled via waveform inversion using a dynamic rupture model, while detection and location techniques are used to better characterize its aftershock sequence. We analyze the local seismotectonic and thermal context of the subducting Nazca plate to understand the trigger mechanism of this earthquake and how it compares with other significant earthquakes in the vicinity. The stress drop and the related dynamic rupture parameters of the Calama mainshock are similar to those of the nearby 2007 M_W 6.8 Michilla and 2015 M_W 6.7 Jujuy inslab earthquakes, which occurred to the west (trenchwards) and to the east (under the back-arc) of the Calama earthquake, respectively. The sequences of these three events were located using a 3-D tomographic velocity model. While the Michilla earthquake sequence occurred within the oceanic crust at temperatures of ~250°C, the Calama sequence occurred within the upper oceanic mantle at ~350°C and exhibited a smaller aftershock productivity than Michilla. Additionally, the 3-D tomographic model shows intermediate Vp/Vs ratios (1.72−1.76) in the region of the Calama earthquake. This indicates a less hydrated environment that would be responsible for the smaller aftershock productivity of the Calama earthquake.

Keywords

Earthquake dynamics. Earthquake source observations. Seismicity and tectonics. Seismic tomography.

1 Introduction

Seismicity within the subducting oceanic Nazca plate in the central Andes occurs at a wide range of depths and magnitudes. Inslab earthquakes in this region can be as shallow as ~40 km depth, defining a deeper plane of seismicity aligned parallel to the plate interface in northern Chile (Bloch *et al*. 2014; Sippl *et al*. 2018). At depths greater than 60 km, the lack of coupling on the plate interface results in a considerable decrease of thrust earthquakes, and only inslab earthquakes occur, defining a double seismic layer within the Nazca plate that extends to ~140 km depth (Comte *et al*. 1999; Dorbath *et al*. 2008; Sippl *et al*. 2018; Florez & Prieto 2019; Lu *et al*. 2021). Beyond those depths, inslab earthquakes are less frequent and more pervasively distributed within the subducting plate. Most of the recorded $M_W > 7.0$ inslab events in the Andes subduction zone have been deep focus earthquakes within the 550 km and 650 km depth range, including the 1921−1922 earthquakes in northern Peru (Okal & Bina 1994), the 1994 Bolivia earthquake (Kikuchi & Kanamori 1994), and the 2015 earthquake doublets in the Peru-Brazil border (Ruiz *et al.* 2017). The shallower section of the Nazca plate in the central Andes has also ruptured with large inslab earthquakes, such as the 1950 M_S 8.0 Antofagasta and 2005 M_W 7.8 Tarapacá earthquakes (Kausel & Campos 1992; Peyrat *et al*. 2006). Additionally, starting in 2007 and within a period of eight years, two $M_W > 6.5$ inslab earthquakes struck at 40 km and 250 km depth along the −23° parallel (Ruiz & Madariaga 2011; Herrera *et al*. 2017).

In this work, we study the rupture properties of a third inslab event that occurred along the same −23° parallel: the 2020 M_W 6.8 Calama inslab earthquake (Figure 1). Considering the peculiar spatiotemporal distribution of these three major inslab earthquakes, we compare their mainshock properties and aftershock sequences, discussing them within the seismological, thermal, and compositional context within the Nazca plate at latitude −23° in the central Andes. Our aim is to evaluate how these factors could control the mainshock and aftershock characteristics of these events.

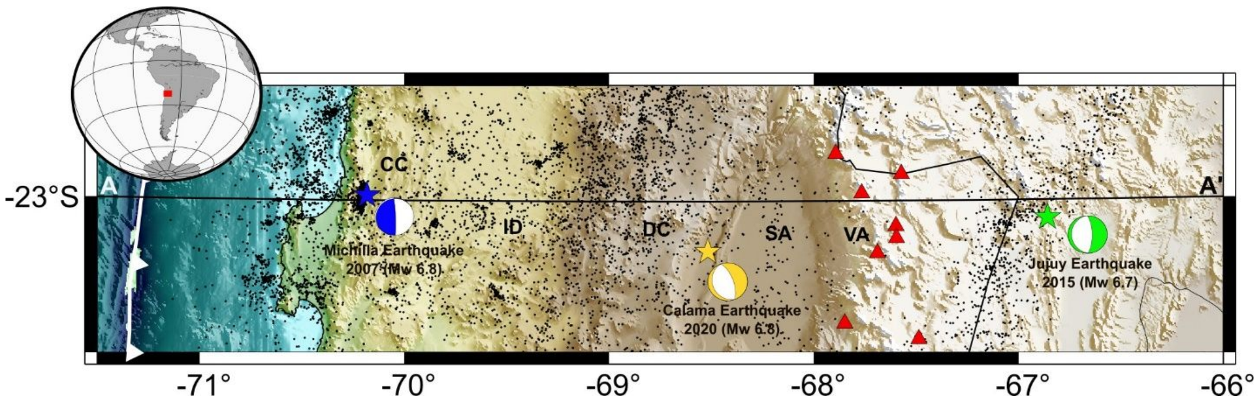

Figure 1: Seismological context of the Calama earthquake. Stars show the epicenters of the Michilla, Calama, and Jujuy earthquakes. Their focal mechanisms from the Global Centroid Moment Tensor (GCMT) catalog (Dziewonski *et al*. 1981; Ekström *et al*. 2012) are also shown. The black dots indicate background seismicity reported by the Centro Sismológico Nacional (CSN) and relocated by Pastén.Araya *et al*. (2018). **CC:** Coastal Cordillera, **ID:** Intermediate Depression, **DC:** Domeyko Cordillera, **SA:** Salar of Atacama, **VA:** Volcanic arc. The red triangles correspond to the main active volcanoes. Cross section A-A' runs along the −23° parallel.

2 The Calama earthquake sequence

The Calama mainshock occurred within the subducting Nazca plate at 123 km depth on June 3, 2020. Its epicenter was located at latitude −23.247° and longitude −68.53°, near the city of Calama in northern Chile, as reported by the Centro Sismológico Nacional (CSN) of the Universidad de Chile. The focal mechanism solution reported by the Global Centroid Moment Tensor (GCMT) catalog (Dziewonski *et al*. 1981; Ekström *et al*. 2012) shows that the rupture occurred on a normal fault (see Figure 1).

Several local strong motion and broadband seismic stations were operational at the time of the Calama earthquake. To carry out all the analyses shown in this work, we use strong motion and broadband waveforms from multiparametric stations of the Integrated Plate boundary Observatory Chile network (IPOC) (GFZ & CNRS-INSU 2006) and the CSN Network (Barrientos & National Seismological Center (CSN) Team 2018). Strong motion waveforms from the network of earthquake-triggered accelerometers of the CSN (Barrientos & National Seismological Center (CSN) Team 2018) are also available.

2.1 Earthquake detection and location

2.1.1 Earthquake detection using template matching

We use template matching (Gibbons & Ringdal 2006) to detect unreported earthquakes around the Calama mainshock. This was done by analyzing continuous broadband velocity waveforms of nine stations near the epicenter from the IPOC and CSN networks (Figure S1a in the Supplementary Material). We used the three components of these stations and bandpass filtered the data from 5 to 30 Hz, because this frequency range exhibits better signal-to-noise ratios (Cabrera et al., 2021). The template events are earthquakes reported by the CSN that occurred within a defined space-time window around the Calama earthquake. When defining a space-time window, a large window might allow the inclusion of additional events, but also more background seismicity that may not be related to the target sequence. By contrast. a smaller window mitigates this effect, but it is more susceptible to miss some events (e.g., Dascher-Cousineau *et al*. 2020; Cabrera *et al*. 2021). To determine the size of the region enclosing the seismicity of the Calama sequence, we followed the expression proposed by Dascher-Cousineau *et al*. (2020) based on the source radius estimated by Wells & Coppersmith (1994), resulting in a radius of 21 km around the hypocenter. In terms of time, we scanned the waveforms from one month before to one month after the mainshock (between May 3, 2020, and July 3, 2020), since this is the maximum number of days for which the nine stations were operating continuously. This space-time window comprises the mainshock and 26 earthquakes (Dataset S1 in the Supplementary Material), where all of them occurred after the mainshock. The waveforms of each template event were extracted by cutting the continuous data 0.5 s before the P-wave arrival and 5 s after the S-wave arrival. Wave arrivals were estimated using a local 1-D velocity model (Husen *et al*. 1999). The length of templates was defined in this way due to the difficulty of estimating P-wave arrivals accurately, given the limitations of the 1-D velocity model (e.g., Frank *et al*. 2017; Cabrera *et al*. 2021). To avoid detection of distant events not related to the studied sequence, correlation coefficients between the template waveforms and the continuous data were calculated within a sliding window that preserves the seismic moveouts using the Fast Matched Algorithm (Beaucé *et al*. 2018) and a GPU-architecture. This resulted in time series that represent the similarity of the continuous data with every single template. We used a threshold of 12 times the median absolute deviation (MAD) of the correlation function, which was averaged over all stations and channels to define the detection of an earthquake significantly similar to the template. The events detected with this criterion are assumed to occur at the same hypocentral location as their template (determined by the CSN), and their magnitudes were estimated by computing the median amplitude ratio between the template event and the aftershock over the considered stations, assuming that a tenfold increase in amplitude corresponds to one unit increase in magnitude (Peng & Zhao 2009). The resulting earthquake dataset of the Calama sequence now includes 108 events in the magnitude range of 0.8−6.8, including templates (Dataset S2). Figure S1b shows the comparison of the frequency-magnitude diagrams between the initial catalog and the new catalog. A higher number of event detections is observed for M < ~3.5, which is the completeness magnitude of the CSN catalog (Barrientos & National Seismological Center (CSN) Team 2018). Figure S1c summarizes the normalized waveforms of all the events in the new catalog recorded at station AF01, which is the closest to the epicenter (see Figure S1a). No earthquakes were detected before the mainshock. The new catalog of the Calama sequence features only aftershocks (see Figure S1d).

2.1.2 Location of the mainshock and aftershocks

To obtain a better resolution of the possible fault plane, we located some of the new aftershocks that were previously detected with template matching. The location was carried out using the same stations that were used for template matching (Figure S1a). First, the arrival times of the P and S waves were manually picked using the SEISAN software (Havskov & Ottemöller 1999). Due to high noise level in the waveforms and limitations on station coverage, only the mainshock and 37 aftershocks could be reliably located. Once the arrival times were determined, the location was performed using the LocIn software (Potin 2016) on a regional 3-D tomographic velocity model (Pastén-Araya *et al.* 2021; Contreras-Reyes *et al.* 2021) (Figure 2). Location results indicate that the hypocenter of the Calama mainshock occurred at 113 km depth. Aftershocks were located mostly updip from the hypocenter, between 100 km and 113 km deep, defining a subvertical rupture plane, consistent with the NE dipping fault plane (strike=333°; dip=60°; rake=−91°) of the GCMT focal mechanism (Figures 1 and 2).

The same location method was applied for both the 2007 M_W 6.8 Michilla and 2015 M_W 6.7 Jujuy sequences, whose mainshock depths were previously reported at 43 km and 254 km, respectively (Ruiz & Madariaga 2011; Pastén-Araya *et al*. 2018; Herrera *et al*. 2017). Our location results show mainshock hypocentral depths of 43 km for Michilla and 228 km for Jujuy. Compared with the Michilla earthquake, location uncertainties are larger for the Calama and Jujuy events, since they occurred at greater depths and were located with a smaller number of available stations, with important azimuthal gaps (Table 1 and Figure S2a). The located aftershock sequences of these two earthquakes exhibit nearly vertical spatial distributions, closely aligned with the orientations of the steeper east-dipping fault planes of their respective focal mechanisms (Figures 1 and 2). These results are also consistent with the aftershock distributions and the selected fault planes reported in the aforementioned studies. We also carried out a relocation of these events using a double-difference method. Although double-difference relocations tend to be slightly deeper (< 2 km) and slightly more clustered (Figure S2b), results are similar to the trends obtained with the absolute location approach.

Table 1: Location of the Michilla, Calama, and Jujuy earthquakes. These hypocenters were inferred in this work based on a 3-D velocity model. Their absolute errors were estimated based on the 90% confidence level.

Event	Origin time	Lon. (°)	Lat. (°)	Depth (km)	RMS (s)	N° of stations	Azimuthal gap (°)	Horizontal error (km)	Vertical error (km)
Michilla	2007-12-16 08:09:17.28	−70.1828	−22.9962	43.5	0.05	24	81	2.5	3.0
Calama	2020-06-03 07:35:34.82	−68.5173	−23.2502	113.4	0.73	9	174	8.0	12.0
Jujuy	2015-02-11 18:57:20.3	−66.8584	−23.0936	228.7	0.8	13	193	9.0	14.0

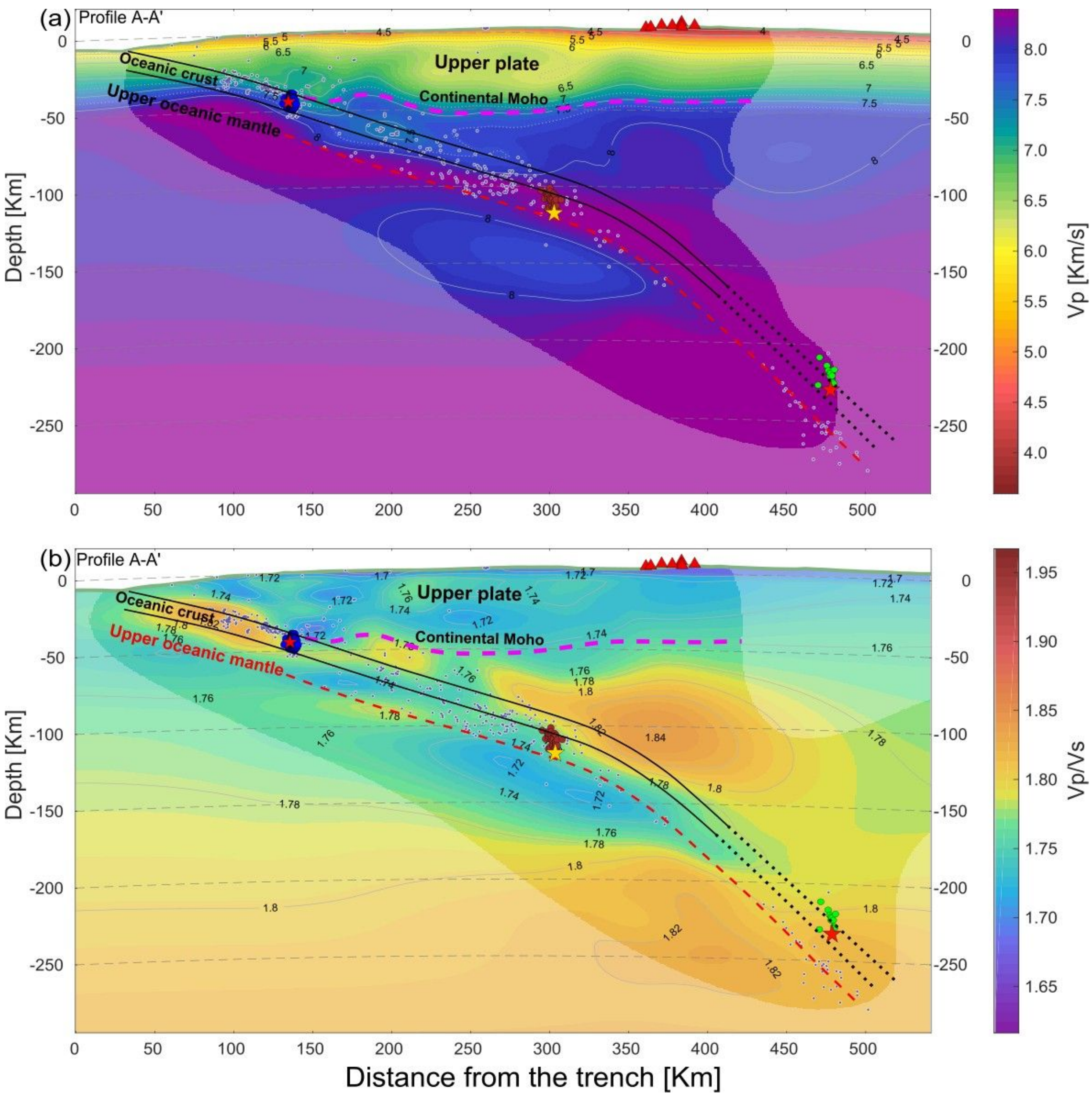

Figure 2: Seismicity within the 3-D tomographic model. (a) Vp and (b) Vp/Vs tomography models (Pastén-Araya *et al.* 2021) along cross section A-A' of Figure 1. Hypocenters of the Calama mainshock and its aftershocks are shown with a yellow star and red circles, respectively. Red stars indicate the hypocenters of the Michilla and Jujuy earthquakes, and their aftershocks are shown with blue and green circles, respectively. The continental Moho was inferred by Tassara & Echaurren (2012). The plate interface as defined by Hayes *et al.* (2018) is shown by the continuous

black line. The oceanic Moho defining the low limit of the oceanic crust was inferred by Contreras-Reyes et al. (2021). The oceanic crust is not accurately resolved below certain depths (segmented line extensions). The red segmented line was defined based on the lower plane of seismicity reported by Sippl *et al*. (2018). Red triangles show the main active volcanoes. The discolored areas of the tomographic model are regions of lower resolution.

2.2 The Calama mainshock

Strong motion data were used to analyze both the ground shaking characteristics of the Calama mainshock and its rupture properties. This earthquake generated a maximum peak ground acceleration (PGA) of 0.13 g at the closest station (hypocentral distance of 132 km). In general, the observed ground shaking intensities are within the ranges predicted by current ground motion models for Chilean inslab earthquakes (see Text S1 and Figure S3 in the Supplementary Material). The low frequency rupture properties of the mainshock were inferred via inversion using a finite-fault model. Following the method used to model the Michilla and Jujuy earthquakes (Ruiz & Madariaga 2011; Herrera *et al*. 2017), the rupture model used in this work assumes an elliptical coseismic slip distribution with semi-axes *a* and *b*, centered at (x_0, y_0) within the fault plane. This ellipse is also allowed to rotate around its center. The rupture nucleates at the hypocenter within a circular area. The overall rupture propagation in this model is controlled by a slip-weakening friction law (Ida 1972). This allows the determination of dynamic rupture parameters, such as: stress drop (T_e), yield stress (T_μ), slip-weakening distance (D_c), and a nucleation of radius R' with a stress T_μ' acting inside it (Madariaga & Ruiz 2016). The finite fault was centered at the hypocenter and was oriented using the strike, dip, and rake of the NE-dipping plane of the focal mechanism reported by GCMT, as suggested by the spatial distribution of the located aftershocks.

Prior to inversion, the baseline-corrected acceleration waveforms were integrated to velocity and filtered between 0.02 and 0.1 Hz with a Butterworth bandpass filter. Finally, the horizontal channels were rotated into radial and transverse components. To create the modeled waveforms, the wave propagation was simulated with the AXITRA code (Bouchon 1981; Coutant 1989) based on a 1-D velocity model (Husen *et al*. 1999). The inversion was performed using the Neighborhood Algorithm (Sambridge 1999), which in this case minimizes the misfit (χ^2) to find the best fitting model:

$$\chi^2 = \frac{\sum_i (obs_i - pred_i)^2}{\sum_i obs_i^2}$$

which runs over the samples *i* of the observed (obs_i) and predicted ($pred_i$) waveforms. The three components (radial, transverse, and vertical) were used in the inversion.

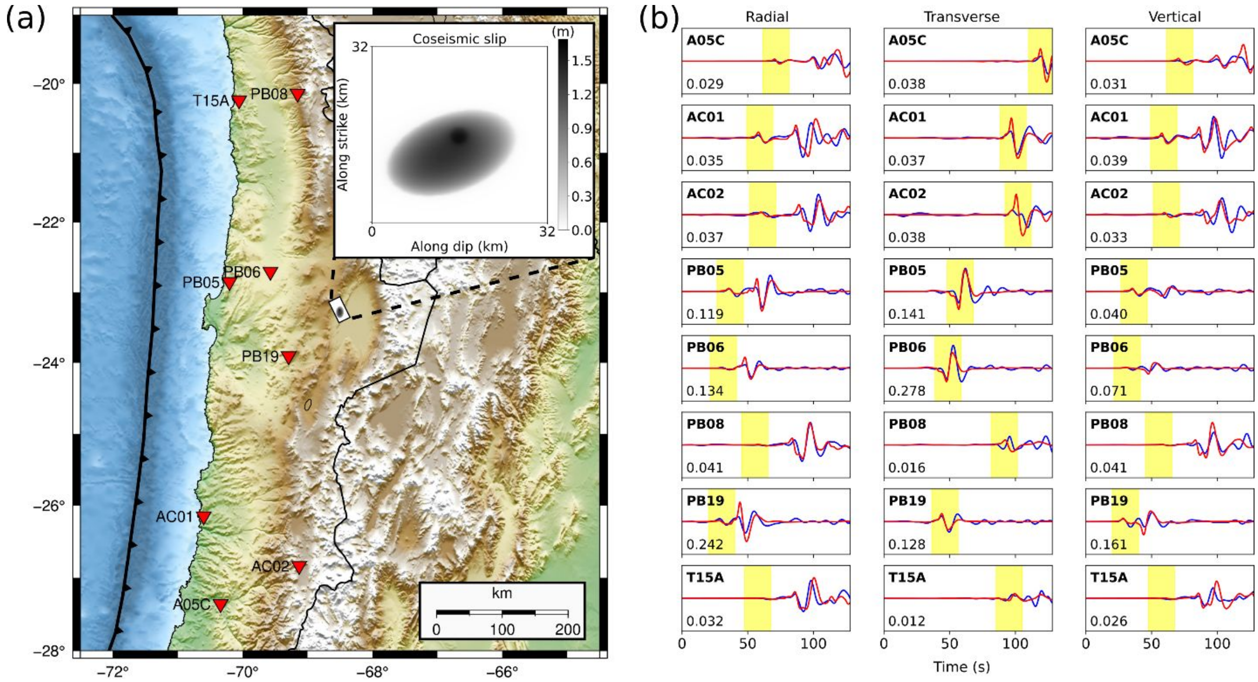

Figure 3: Dynamic modeling of the Calama earthquake. (a) Map showing the stations used for the modeling. The inset plot shows the best coseismic slip distribution of the Calama earthquake, zoomed from its epicentral location. (b) Observed (blue) and predicted (red) waveforms associated to the best dynamic model. Sections highlighted in yellow comprise the P waves (radial and vertical components) and SH waves (transverse component). The number within each plot is the maximum waveform amplitude (m/s).

Due to the limitations of the 1-D velocity model, waveforms of a subset of eight stations around the epicenter were used for modeling (stations shown in Figure 3a). The Neighborhood Algorithm converged to a best dynamic rupture model that has a maximum coseismic slip of 1.59 m. The two axes of this elliptical model are 14.1 km and 24.4 km long (Figure 3a), with a rupture time of 5.6 s. Dynamically, the overall rupture had a T_e = 10.1 MPa, T_μ = 11.9 MPa, and nucleated within a circle of R' = 1.46 km with T_μ' = 15.4 MPa inside. A distance D_c = 0.7 m was required to nucleate the rupture. The model parameters started to converge around these optimal values roughly after 10,000 sampled models (Figure S4). Parameter distributions and their uncertainties around these optimal values are shown in Figure S5. Some model parameters (e.g., b, y_0, T_e, T_u', and D_c) are less Gaussian-distributed than others, which could indicate trade-offs between them. In particular, the correlation is stronger between the stresses (Figure S6), since in the model formulation, T_μ and T_μ' depend on T_e. If the full seismograms are considered, the overall misfit associated to the best dynamic model is 0.58. In this case, the high-amplitude SV waves in the radial and vertical components could not be properly modeled in some stations (Figure 3b), resulting in this large misfit. This is likely due to converted body and surface waves arriving behind the SV waves, which could be generated by structures that are not represented by a simple 1-D velocity model. A similar case was shown by Herrera *et al*. (2017) for the Jujuy earthquake that occurred further east. Following their formulation, if the misfit is calculated using only P and high-amplitude SH waves (highlighted seismogram sections in Figure 3b), its value is reduced to 0.24. This is the misfit formulation that was minimized in the inversion to obtain the described best dynamic model of the Calama earthquake.

3 Discussion

3.1 Comparing dynamic properties of mainshock ruptures

The Calama mainshock was modeled using a finite-fault model, where the rupture propagation is controlled by a slip-weakening friction law. The other two mainshocks at Michilla and Jujuy were previously modeled using the same dynamic rupture model and inversion method (Ruiz & Madariaga 2011; Herrera *et al*. 2017). This allows a comparison of the inferred dynamic parameters with no bias related to differences in methods. The dynamic rupture parameters are summarized in Table 2, including the similarity parameter κ (Madariaga & Olsen 2000), calculated assuming the characteristic rupture size as the average of the ellipse semi-axes.. All dynamic parameters of these three earthquakes are rather similar. In particular, the stress drop does not seem to be correlated with depth, which has also been observed with global earthquake databases (Poli & Prieto 2016). Overall, the T_e values of these three events fall within the empirically estimated ranges for inslab earthquakes globally (e.g., Kanamori & Anderson 1975; Poli & Prieto 2016), and they are larger than the T_e values of thrust earthquakes inferred with the same method in northern Chile (Otarola *et al*. 2021).

Table 2: Comparison of the best dynamic models of the Michilla, Calama, and Jujuy earthquakes. For the Calama earthquake, values of their posterior mean and standard deviation are also shown in parenthesis.

Parameter	**Michilla**	**Calama**	**Jujuy**
Semi axis a (km)	4.0	7.08 (7.05±0.04)	7.94
Semi axis b (km)	10.12	12.21 (12.24±0.05)	4.87
Center x_0 (km)	0.85	12.83 (12.95±0.1)	12.71
Center y_0 (km)	-2.0	14.56 (14.82±0.26)	11.63
Rotation angle (°)	85.9	159.8 (162±1.8)	203.4
T_e (MPa)	14.97	10.05 (9.86±0.14)	11.87
T_u (MPa)	19.18	11.87 (11.81±0.12)	14.37
T_u' (MPa)	23.65	15.35 (15.11±0.25)	16.1
R' (km)	0.98	1.46 (1.47±0.01)	1.09
D_c (m)	0.65	0.7 (0.67±0.02)	0.41
κ	2.08	1.5 (1.53±0.02)	1.97

3.2 The Calama earthquake occurrence within the upper oceanic mantle

Inslab earthquakes mostly occur in double seismic zones (DSZ), which has been observed in different subduction zones (Brudzinski *et al*. 2007). This DSZ is characterized by an upper seismicity plane (USP) located in the oceanic crust and a lower seismicity plane (LSP) located 20-40 km below the USP in the upper oceanic mantle. The subduction zone of northern Chile is not an exception, and this DSZ has also been recognized in that region (Comte *et al*. 1999; Rietbrock & Waldhauser 2004, Bloch *et al*. 2014; Sippl *et al*. 2018; Florez & Prieto 2019; Lu *et al*. 2021). For example, the mainshock and aftershocks of the Calama sequence located in this work are concentrated between 100 km and 113 km depth, indicating that the rupture occurred in the LSP within the oceanic mantle, below the oceanic Moho (Figure 4). In contrast, the location results of the Michilla sequence indicate that its rupture occurred in the USP within the oceanic crust (Figure 4).

Different mechanisms have been proposed for the generation of inslab seismicity (e.g., Frohlich 2006; Houston 2015). For the seismicity located in the USP within the oceanic crust, there is a consensus that it could be related to the presence of fluids linked to dehydration processes within the oceanic crust at different pressures and temperatures (e.g., Kirby 1995; Hacker *et al*. 2003). Dehydration might cause the reduction of the effective normal stress, promoting brittle rupture of structures inherited from the faulting process in the outer-rise zone prior to subduction (Ranero *et al*. 2005; Ruiz & Contreras-Reyes 2015; Pastén-Araya *et al*. 2018; Cabrera *et al*. 2021). However, the mechanisms that generate inslab seismicity at the LSP are still a subject of debate (Duesterhoeft *et al*. 2014; Ferrand *et al*. 2017; Ohuchi *et al*. 2017; Scambelluri *et al*. 2017). Mechanisms that point to a hydrated lithospheric oceanic mantle have been proposed to trigger seismicity in the LSP (Bloch *et al*. 2018; Cai *et al*. 2018). On the other hand, analysis of laboratory and field data suggests that faulting could be triggered in dry rocks within a partially hydrated oceanic

283 lithospheric mantle (Ferrand *et al*. 2017; Kita & Ferrand 2018). This process has been referred to
284 as dehydration-driven stress transfer, which would not require the presence of a highly hydrated
285 lithospheric mantle. Instead, a rupture could nucleate in a weakly hydrated portion of the
286 lithosphere and propagate to dry regions of the lithosphere due to the stress transfer associated to
287 volumetric change of the rock. Additionally, Florez & Prieto (2019) found that globally, LSP
288 seismicity have consistently smaller *b*-values compared with the USP seismicity, which would
289 also indicate a relatively dry environment in the LSP.

290 According to hydrological and numerical models, dehydration of the subducted slab occurs mainly
291 in three stages (Ulmer & Trommsdorff 1995; Peacock 2001; Hacker *et al.* 2003; Rüpke *et al.*
292 2004). First, dewatering of subducting sediments leads to hydration of the mantle wedge at depths
293 < 20 km (ANCORP Working Group 1999, Rüpke *et al.* 2004). Second, metamorphic dehydration
294 reactions of the subducting oceanic crust increase pore pressure and decrease effective confining
295 pressure, thereby promoting inslab seismicity (60−80 km depth) (Peacock 2001; Hacker *et al.*
296 2003). Third, at depths larger than 100 km, the subducting lithospheric mantle dehydrates (Rüpke
297 *et al.* 2004) and triggers inslab seismicity (Yuan *et al.* 2000; Peacock 2001) causing partial melting
298 and leading to arc volcanism (Rüpke *et al.* 2004; Contreras-Reyes *et al.* 2021). In our study case,
299 dehydration reactions of the upper oceanic mantle are consistent with a zone of intermediate Vp/Vs
300 ratios (1.72−1.76) in the region of the Calama earthquake (Figure 2b). This zone also presents
301 "typical" uppermost mantle Vp values of ~8.3 km/s (Figure 2a) at > 600 MPa, suggesting the
302 presence of dry dunite/peridotite mantle rocks (Christensen 1996). In addition, the mantle wedge
303 presents large Vp/Vs ratios of 1.8−1.84 above the location of the Calama earthquake, which
304 indirectly indicates the occurrence of massive dehydration reactions from the subducting oceanic
305 lithosphere (e.g., Rüpke et al., 2004).

306 In summary, our results indicate that the Calama earthquake is likely a good example of an event triggered by the dehydration-driven stress transfer mechanism in dryer conditions. By contrast, the Michilla earthquake occurred within the oceanic crust where Vp/Vs > 1.8 (Figure 2b), suggesting that the presence of fluids and a reduction of the effective normal stress could favor earthquake occurrence. The oceanic crust cannot be resolved in the region of the Jujuy earthquake. Moreover, the tomographic model cannot resolve Vp/Vs properly beyond 150−180 depth (Figure 2b). Therefore, considering this and the location uncertainties of the Jujuy earthquake (see Table 1 and Figure S2), for now the available data shows that this event occurred somewhere within the uppermost oceanic lithosphere, likely at lithostatic pressures of about 7 GPa and estimated temperatures of 300°C−600°C (Figure 4). At these P-T conditions, the uppermost oceanic/subducting lithosphere dehydrates, favoring brittle faulting (Rüpke et al., 2004).

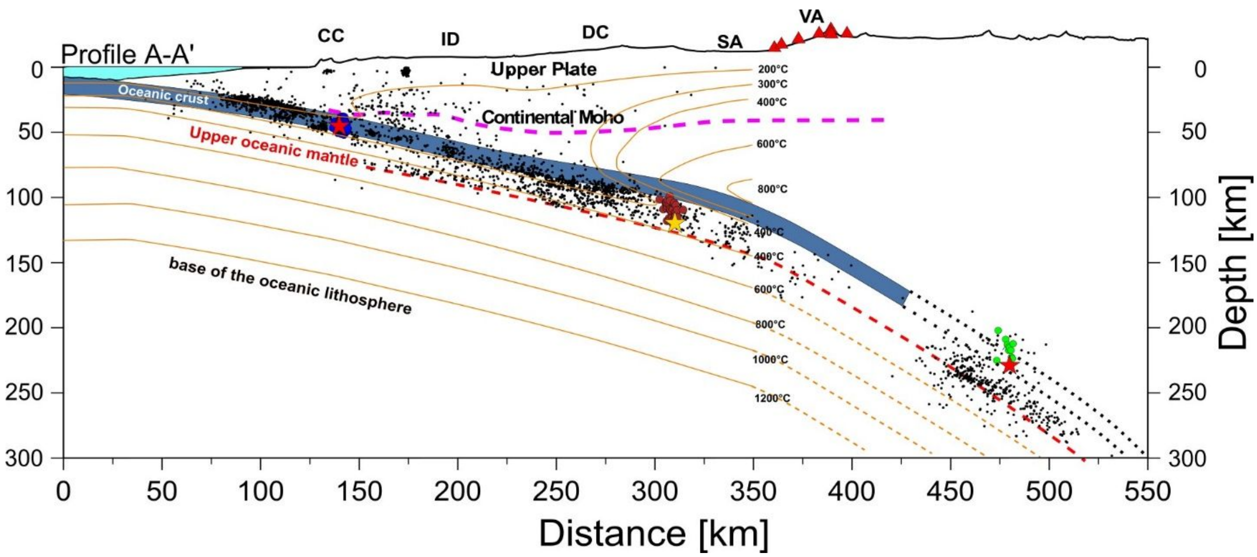

Figure 4: Cross section A-A'. Symbols of the Michilla, Calama, and Jujuy earthquakes and their aftershocks are as described in Figure 2. The black dots indicate background seismicity at the area reported by the CSN and by Pastén.Araya *et al*. (2018). The continental Moho was inferred by Tassara & Echaurren (2012). The orange isotherms correspond to the thermal model of northern Chile (Cabrera *et al*. 2021). The slab geometry is the Slab2.0 (Hayes *et al*. 2018). The oceanic crust and isotherms are not accurately resolved below certain depths (segmented line extensions). **CC:** Coastal Cordillera, **ID:** Intermediate Depression, **DC:** Domeyko Cordillera, **SA:** Salar of Atacama, **VA:** Volcanic arc. The red triangles correspond to the main active volcanoes. The base of the oceanic lithosphere at ~1200°C is based on Richards et al. (2018).

3.3 Thermal conditions and aftershock rate

Several studies have suggested that temperature could be an important factor that controls the distribution of both thrust and inslab seismicity (Oleskevich *et al*. 1999; Wang *et al*. 2015; Wei *et al*. 2017; Liu *et al*. 2021). To try to establish the degree of influence of temperature on the Calama sequence, as well as on the other two inslab earthquakes, we used the thermal model of northern

Chile proposed by Cabrera *et al*. (2021), which is well defined between the trench and the volcanic arc in the upper ~200 km (Figure 4). Clear common trends are observed between the isotherms and the seismicity distribution. While the thrust seismicity is concentrated along the 200°C isotherm, the inslab seismicity defined by the DZS is mostly concentrated between the 300°C and 400°C isotherms. A decrease in the seismicity is observed at higher temperatures, which could indicate a transition from brittle to ductile behavior at greater depths below the 500°C−600°C isotherm along the subducting plate, particularly in the zones of the Michilla and Calama earthquakes. The brittle/ductile transition in the region of the Jujuy event seems to be deeper across the 600°C−800°C isotherms (Figure 4). Cabrera et al. (2021) studied intermediate-depth seismicity in northern Chile between latitudes −18° and −20° (200−300 km northwards of our study area) and concluded that the neutral surface and brittle/ductile transition zone becomes deeper within the subducting plate at depths of 80−120 km (600°C−800°C). Seismicity in the region of the Jujuy sequence seems to be consistent with these findings (Figure 4).

The Calama sequence occurred between the 300°C and 400°C isotherms (Figure 4), and its aftershocks mostly occurred at shallower depths than the mainshock. Similar trends were observed for the aftershock distributions of the 2019 M_W 6.7 Coquimbo and 2018 M_W 7.1 Anchorage inslab earthquakes, which also exhibited shallower aftershocks than the mainshock (Ruiz *et al*. 2019; Ruppert *et al*. 2020; Liu *et al*. 2019). In particular, the Coquimbo mainshock occurred between the 600°C and 700°C isotherms within the subducting plate (Ruiz *et al*. 2019). However, its aftershocks mostly occurred at shallower (and colder) layers, at temperatures below 450°C. These examples indicate that temperature could play a significant role in the aftershock distribution of intermediate-depth inslab earthquakes, which tend to occur in layers of lower temperatures.

The aftershock productivity of inslab earthquakes is another aspect that is related to both the zone where they are triggered and the temperature. Cabrera *et al*. (2021) carried out an analysis of several inslab earthquakes in northern Chile, finding that inslab earthquakes that occur at greater depths below the 400-450°C isotherms produce very few or no aftershocks, and would be associated with a dry environment. Conversely, those events that occur at shallower depths above the 400°C−450°C isotherms, usually produce more aftershocks and would be associated with a more hydrated environment. Our results corroborate this observation, particularly when comparing the cases of the 2007 Michilla and the 2020 Calama earthquakes, which occurred at depths where the thermal model is still well defined. The Michilla earthquake occurred within the oceanic crust between the 200°C to 300°C isotherms (Figure 4), producing a large number of aftershocks and a zone with persistent seismicity in time (Ruiz & Madariaga 2011; Fuenzalida *et al*. 2013; Pastén-Araya *et al*. 2018). Conversely, the Calama mainshock and its aftershocks occurred in the upper oceanic mantle between the 300°C and 400°C isotherms. Within the first five days after the mainshock, the Calama earthquake produced a much smaller number of $M \geq 2.0$ aftershocks (53 events) compared with the Michilla earthquake (313 events). Therefore, these observations, in combination with the observed differences of Vp/Vs ratios between the Calama and Michilla earthquakes, suggest that the Calama earthquake occurred in a warmer and less hydrated environment than the region of the Michilla earthquake, and would be responsible for its lower aftershock productivity. This is consistent with observations obtained by Chu & Beroza (2022) in the subducting Pacific Plate in Japan. They found that the aftershock productivity is correlated with Vp/Vs ratio, discussing that a high Vp/Vs ratio can be a result of high fluid pressure and a larger number of faults and cracks that could be fluid-filled, or also oriented perpendicular to ray paths.

4 Conclusions

The 2020 M_W 6.8 Calama earthquake is an inslab earthquake that occurred at intermediate depths, at the same latitude (−23°) as the 2007 M_W 6.8 Michilla and 2015 M_W 6.7 Jujuy inslab events. It featured ground shaking intensities that are typical of Chilean inslab earthquakes.

The hypocenter of the Calama earthquake was located at 113 km depth using a 3-D model. The same method was used to locate the hypocenters of the Michilla and Jujuy earthquakes, resulting in depths of 43 km and 228 km, respectively. At their located depths, we observed that the Michilla earthquake occurred within the oceanic crust, while the Calama earthquake occurred within the upper oceanic mantle, below the oceanic crust. The resolution of our database does not allow exact interpretations of the Jujuy earthquake location within the uppermost oceanic lithosphere due to the larger uncertainties in earthquake, slab, and oceanic Moho locations at those depths.

The dynamic properties of the Calama earthquake were inferred through modeling of low-frequency waveforms, which is the same method that was used previously to model the Michilla and Jujuy earthquakes. Despite their different hypocentral depths and locations in different layers of the subducting oceanic plate, the dynamic properties of these three events are similar. Particularly, their stress drop values range between 10 MPa and 15 MPa, within the observed ranges of inslab earthquakes, which are in general larger than stress drop values of thrust earthquakes.

Thermal and pressure conditions of the subducting plate likely control the spatial distribution of inslab seismicity along the −23° parallel in northern Chile, where the 500°C−600°C isotherms along the subducting plate define a limit for inslab seismicity occurrence down to ~150 km depth.

Additionally, the varying water content and thermal conditions of mantle rocks in the areas where inslab earthquakes occur play an important role in their aftershock productivity. For instance, the Michilla earthquake occurred within the oceanic crust at temperatures between 200°C and 300°C, exhibiting a strong aftershock activity. The large Vp/Vs ratio (> 1.8) at that location indicate a more hydrated environment that favors brittle rupture and an increase in aftershocks. On the other hand, the Calama earthquake occurred in the uppermost oceanic mantle, where Vp/Vs ratio is smaller (between 1.72 and 1.76), and temperatures vary between 300°C and 400°C. This earthquake exhibited a smaller aftershock productivity, which is likely a result of a less hydrated environment, as suggested by the reduced Vp/Vs ratios in this region.

Our results show that even though the Michilla and Calama earthquakes occurred in regions of different thermal and compositional characteristics within the Nazca plate, curiously these factors do not significantly affect the dynamic characteristics of the mainshocks, which were found to be within the typical ranges of inslab events. However, they do affect their aftershock productivity. Additional studies with a larger database of well-recorded earthquakes are necessary to confirm if this trend is observed in more events.

Data availability statement

Waveform data from multiparametric stations were downloaded from the International Federation of Digital Seismograph Networks (FDSN) web services using the ObsPy toolkit (Beyreuther *et al*. 2010). Waveforms from the earthquake-triggered network of accelerometers of the CSN can be accessed from their website (evtdb.csn.uchile.cl/). The earthquake catalogs used in this study can

422 be accessed from their respective websites: CSN catalog (www.sismologia.cl), GCMT catalog
423 (www.globalcmt.org). Maps were created using Generic Mapping Tools (Wessel *et al*. 2013).

424

425 **Acknowledgments**

426 The author C. Herrera designed and wrote most of the manuscript. He also carried out the strong
427 motion analysis and the dynamic modeling of the Calama mainshock. F. Pastén-Araya designed
428 and contributed with the discussion that relates the tomography and thermal models with the
429 analyzed earthquake sequences. F. Pastén-Araya and R. Madariaga thank the Programa de Riesgo
430 Sísmico (PRS) of the Universidad de Chile. L. Cabrera carried out the template matching using
431 the University of Grenoble Alpes (UGA) High-Performance Computing infrastructures CIMENT.
432 He was supported by the European Union Horizon 2020 Research and Innovation Programme
433 (grant agreements, 802777-MONIFAULTS). B. Potin and E. Rivera contributed with the location
434 and relocation analyses of the three studied earthquakes and their aftershocks. Part of the
435 computations were performed using the GRICAD infrastructure (https://gricad.univ-grenoble-
436 alpes.fr), which is supported by Grenoble research communities. S. Ruiz, R. Madariaga, and E.
437 Contreras-Reyes contributed with editing assistance and review of the manuscript during
438 preparation. E. Contreras-Reyes also acknowledges the support of PIA/FONDEYT grant 1210101.
439 We finally thank Jörg Renner, Frederik Tilmann, and another anonymous reviewer for their
440 thorough reviews that helped improving this work.

441

442 **References**

ANCORP Working Group., 1999. Seismic reflection image revealing offset of Andean subduction-zone earthquake locations into oceanic mantle. *Nature*, 397(6717), 341. https://doi.org/10.1038/16909

Barrientos, S., & National Seismological Center (CSN) Team, 2018. The seismic network of Chile. *Seismological Research Letters*, 89(2A), 467-474. https://doi.org/10.1785/0220160195

Beaucé, E., Frank, W. B., & Romanenko, A., 2018. Fast matched filter (FMF): An efficient seismic matched-filter search for both CPU and GPU architectures. *Seismological Research Letters*, 89(1), 165-172. https://doi.org/10.1785/0220170181

Beyreuther, M., Barsch, R., Krischer, L., Megies, T., Behr, Y., & Wassermann, J., 2010. ObsPy: A Python toolbox for seismology. *Seismological Research Letters*, 81(3), 530–533. https://doi.org/10.1785/gssrl.81.3.530

Bloch, W., Kummerow, J., Salazar, P., Wigger, P., & Shapiro, S. A., 2014. High-resolution image of the North Chilean subduction zone: seismicity, reflectivity and fluids. *Geophysical Journal International*, 197(3), 1744-1749. https://doi.org/10.1093/gji/ggu084

Bloch, W., John, T., Kummerow, J., Salazar, P., Krüger, O. S., & Shapiro, S. A., 2018. Watching dehydration: Seismic indication for transient fluid pathways in the oceanic mantle of the subducting Nazca slab. *Geochemistry, Geophysics, Geosystems*, 19(9), 3189-3207. https://doi.org/10.1029/2018GC007703

Bouchon, M., 1981. A simple method to calculate Green's functions for elastic layered media. *Bulletin of the Seismological Society of America*, 71(4), 959-971. https://doi.org/10.1785/BSSA0710040959

464 Brudzinski, M. R., Thurber, C. H., Hacker, B. R., & Engdahl, E. R., 2007. Global prevalence of double Benioff zones. *Science*, 316(5830), 1472-1474. https://doi.org/10.1126/science.1139204

466 Cabrera, L., Ruiz, S., Poli, P., Contreras-Reyes, E., Osses, A., & Mancini, R., 2021. Northern Chile intermediate-depth earthquakes controlled by plate hydration. *Geophysical Journal International*, 226(1), 78-90. https://doi.org/10.1093/gji/ggaa565

469 Cai, C., Wiens, D. A., Shen, W., & Eimer, M., 2018. Water input into the Mariana subduction zone estimated from ocean-bottom seismic data. *Nature*, 563(7731), 389-392. https://doi.org/10.1038/s41586-018-0655-4

472 Christensen, N. I., 1996. Poisson's ratio and crustal seismology. *Journal of Geophysical Research: Solid Earth*, 101(B2), 3139-3156. https://doi.org/10.1029/95JB03446

474 Chu, S. X., & Beroza, G. C., 2022. Aftershock productivity of intermediate-depth earthquakes in Japan. *Geophysical Journal International*, 230(1), 448-463. https://doi.org/10.1093/gji/ggac024

476 Comte, D., Dorbath, L., Pardo, M., Monfret, T., Haessler, H., Rivera, L., Frogneux, M., Glass, B., & Meneses, C., 1999. A double-layered seismic zone in Arica, northern Chile. *Geophysical Research Letters*, 26(13), 1965-1968. https://doi.org/10.1029/1999GL900447

479 Contreras-Reyes, E., Díaz, D., Bello-González, J. P., Slezak, K., Potin, B., Comte, D., Maksymowicz, A., Ruiz, J. A., Osses, A., & Ruiz, S., 2021. Subduction zone fluids and arc magmas conducted by lithospheric deformed regions beneath the central Andes. *Scientific reports*, 11(1), 1-12. https://doi.org/10.1038/s41598-021-02430-9

483 Coutant, O., 1989. Programme de simulation numérique AXITRA, Rapport LGIT, Universite Joseph Fourier, Grenoble, France.

Dascher-Cousineau, K., Brodsky, E. E., Lay, T., & Goebel, T. H., 2020. What controls variations in aftershock productivity?. *Journal of Geophysical Research: Solid Earth*, 125(2), e2019JB018111. https://doi.org/10.1029/2019JB018111

Dorbath, C., Gerbault, M., Carlier, G., & Guiraud, M., 2008. Double seismic zone of the Nazca plate in northern Chile: High-resolution velocity structure, petrological implications, and thermomechanical modeling. *Geochemistry, Geophysics, Geosystems*, 9(7). https://doi.org/10.1029/2008GC002020

Duesterhoeft, E., Quinteros, J., Oberhänsli, R., Bousquet, R., & de Capitani, C., 2014. Relative impact of mantle densification and eclogitization of slabs on subduction dynamics: A numerical thermodynamic/thermokinematic investigation of metamorphic density evolution. *Tectonophysics*, 637, 20-29. https://doi.org/10.1016/j.tecto.2014.09.009

Dziewonski, A. M., Chou, T. A., & Woodhouse, J. H., 1981. Determination of earthquake source parameters from waveform data for studies of global and regional seismicity. *Journal of Geophysical Research: Solid Earth*, 86(B4), 2825-2852. https://doi.org/10.1029/JB086iB04p02825

Ekström, G., Nettles, M., & Dziewoński, A. M., 2012. The global CMT project 2004–2010: Centroid-moment tensors for 13,017 earthquakes. *Physics of the Earth and Planetary Interiors*, 200, 1-9. https://doi.org/10.1016/j.pepi.2012.04.002

Ferrand, T. P., Hilairet, N., Incel, S., Deldicque, D., Labrousse, L., Gasc, J., Renner, J., Wang, Y., Green II, H. W., & Schubnel, A., 2017. Dehydration-driven stress transfer triggers intermediate-depth earthquakes. *Nature communications*, 8(1), 1-11. https://doi.org/10.1038/ncomms15247

Florez, M. A., & Prieto, G. A., 2019. Controlling factors of seismicity and geometry in double seismic zones. *Geophysical Research Letters*, 46(8), 4174-4181. https://doi.org/10.1029/2018GL081168

Frank, W. B., Poli, P., & Perfettini, H., 2017. Mapping the rheology of the central Chile subduction zone with aftershocks. *Geophysical Research Letters*, 44(11), 5374-5382. https://doi.org/10.1002/2016GL072288

Frohlich, C., 2006. *Deep Earthquakes*. Cambridge: Cambridge University Press. https://doi.org/10.1017/CBO9781107297562

Fuenzalida, A., Schurr, B., Lancieri, M., Sobiesiak, M., & Madariaga, R., 2013. High-resolution relocation and mechanism of aftershocks of the 2007 Tocopilla (Chile) earthquake. *Geophysical Journal International*, 194(2), 1216-1228. https://doi.org/10.1093/gji/ggt163

GFZ, & CNRS-INSU, 2006. IPOC Seismic Network. Integrated Plate boundary Observatory Chile – IPOC. Other/Seismic Network. https://doi.org/10.14470/PK615318

Gibbons, S. J., & Ringdal, F., 2006. The detection of low magnitude seismic events using array-based waveform correlation. *Geophysical Journal International*, 165(1), 149-166. https://doi.org/10.1111/j.1365-246X.2006.02865.x

Havskov, J., & Ottemöller, L., 1999. SeisAn earthquake analysis software. *Seismological Research Letters*, 70(5), 532-534. https://doi.org/10.1785/gssrl.70.5.532

Hacker, B. R., Peacock, S. M., Abers, G. A., & Holloway, S. D., 2003. Subduction factory 2. Are intermediate-depth earthquakes in subducting slabs linked to metamorphic dehydration reactions?. *Journal of Geophysical Research: Solid Earth*, 108(B1). https://doi.org/10.1029/2001JB001129

Hayes, G. P., Moore, G. L., Portner, D. E., Hearne, M., Flamme, H., Furtney, M., & Smoczyk, G. M., 2018. Slab2, a comprehensive subduction zone geometry model. *Science*, 362(6410), 58-61. https://doi.org/10.1126/science.aat4723

Herrera, C., Ruiz, S., Madariaga, R., & Poli, P., 2017. Dynamic inversion of the 2015 Jujuy earthquake and similarity with other intraslab events. *Geophysical Journal International*, 209(2), 866-875. https://doi.org/10.1093/gji/ggx056

Houston, H., 2015. Deep earthquakes, in *Treatise on Geophysics*, pp. 329-354, ed. Schubert, G., Elsevier.

Husen, S., Kissling, E., Flueh, E., & Asch, G., 1999. Accurate hypocentre determination in the seismogenic zone of the subducting Nazca Plate in northern Chile using a combined on-/offshore network. *Geophysical Journal International*, 138(3), 687-701. https://doi.org/10.1046/j.1365-246x.1999.00893.x

Ida, Y., 1972. Cohesive force across the tip of a longitudinal-shear crack and Griffith's specific surface energy. *Journal of Geophysical Research*, 77(20), 3796-3805. https://doi.org/10.1029/JB077i020p03796

Kanamori, H., & Anderson, D. L., 1975. Theoretical basis of some empirical relations in seismology. *Bulletin of the Seismological Society of America*, 65(5), 1073-1095.

Kausel, E., & Campos, J., 1992. The Ms = 8 tensional earthquake of 9 December 1950 of northern Chile and its relation to the seismic potential of the region. P*hysics of the earth and planetary interiors*, 72(3-4), 220-235. https://doi.org/10.1016/0031-9201(92)90203-8

547 Kikuchi, M., & Kanamori, H., 1994. The mechanism of the deep Bolivia earthquake of June 9, 1994. *Geophysical Research Letters*, 21(22), 2341-2344. https://doi.org/10.1029/94GL02483

549 Kirby, S., 1995. Interslab earthquakes and phase changes in subducting lithosphere. *Reviews of Geophysics*, 33(S1), 287-297. https://doi.org/10.1029/95RG00353

551 Kita, S., & Ferrand, T. P., 2018. Physical mechanisms of oceanic mantle earthquakes: Comparison of natural and experimental events. *Scientific reports*, 8(1), 1-11. https://doi.org/10.1038/s41598-018-35290-x

554 Liu, C., Lay, T., Xie, Z., & Xiong, X., 2019. Intraslab deformation in the 30 November 2018 Anchorage, Alaska, MW 7.1 earthquake. *Geophysical Research Letters*, 46(5), 2449-2457. https://doi.org/10.1029/2019GL082041

557 Liu, H., Gurnis, M., Leng, W., Jia, Z., & Zhan, Z., 2021. Tonga Slab Morphology and Stress Variations Controlled by a Relic Slab: Implications for Deep Earthquakes in the Tonga-Fiji Region. *Geophysical Research Letters*, 48(7), e2020GL091331. https://doi.org/10.1029/2020GL091331

561 Lu, P., Zhang, H., Gao, L., & Comte, D., 2021. Seismic imaging of the double seismic zone in the subducting slab in Northern Chile. *Earthquake Research Advances*, 1(1), 100003. https://doi.org/10.1016/j.eqrea.2021.100003

564 Madariaga, R., & Olsen, K., 2000. Criticality of Rupture Dynamics in 3-D. *Pure and Applied Geophysics*. 157, 1981–2001. https://doi.org/10.1007/PL00001071

566 Madariaga, R., & Ruiz, S., 2016. Earthquake dynamics on circular faults: A review 1970–2015. *Journal of Seismology*, 20(4), 1235-1252. https://doi.org/10.1007/s10950-016-9590-8

Ohuchi, T., Lei, X., Ohfuji, H., Higo, Y., Tange, Y., Sakai, T., Fujino, K., & Irifune, T., 2017. Intermediate-depth earthquakes linked to localized heating in dunite and harzburgite. *Nature Geoscience*, 10(10), 771-776. https://doi.org/10.1038/ngeo3011

Okal, E. A., & Bina, C. R., 1994. The deep earthquakes of 1921–1922 in northern Peru. *Physics of the Earth and Planetary Interiors*, 87(1-2), 33-54. https://doi.org/10.1016/0031-9201(94)90020-5

Oleskevich, D. A., Hyndman, R. D., & Wang, K., 1999. The updip and downdip limits to great subduction earthquakes: Thermal and structural models of Cascadia, south Alaska, SW Japan, and Chile. *Journal of Geophysical Research: Solid Earth*, 104(B7), 14965-14991. https://doi.org/10.1029/1999JB900060

Otarola, C., Ruiz, S., Herrera, C., Madariaga, R., & Siegel, C., 2021. Dynamic rupture of subduction earthquakes located near the trench. *Earth and Planetary Science Letters*, 562, 116842. https://doi.org/10.1016/j.epsl.2021.116842

Pastén-Araya, F., Salazar, P., Ruiz, S., Rivera, E., Potin, B., Maksymowicz, A., Torres, E., Villarroel, J., Cruz, E., Valenzuela, J., Jaldín, D., González, G., Bloch, W., Wigger, P., & Shapiro, S. A., 2018. Fluids along the plate interface influencing the frictional regime of the Chilean subduction zone, northern Chile. *Geophysical Research Letters*, 45(19), 10-378. https://doi.org/10.1029/2018GL079283

Pastén-Araya, F., Potin, B., Ruiz, S., Zerbst, L., Aden-Antoniów, F., Azúa, K., Rivera, E., Rietbrock, A., Salazar, P., & Fuenzalida, A., 2021. Seismicity in the upper plate of the Northern Chilean offshore forearc: Evidence of splay fault south of the Mejillones Peninsula. *Tectonophysics*, *800*, 228706. https://doi.org/10.1016/j.tecto.2020.228706

Peacock, S. M., 2001. Are the lower planes of double seismic zones caused by serpentine dehydration in subducting oceanic mantle?. *Geology*, 29(4), 299-302. https://doi.org/10.1130/0091-7613(2001)029<0299:ATLPOD>2.0.CO;2

Peng, Z., & Zhao, P., 2009. Migration of early aftershocks following the 2004 Parkfield earthquake. *Nature Geoscience*, 2(12), 877-881. https://doi.org/10.1038/ngeo697

Peyrat, S., Campos, J., De Chabalier, J. B., Perez, A., Bonvalot, S., Bouin, M. P., Legrand, D., Nercessian, A., Charade, O., Patau, G., Clévédé, E., Kausel, E., Bernard, P., & Vilotte, J. P., 2006. Tarapacá intermediate-depth earthquake (Mw 7.7, 2005, northern Chile): A slab-pull event with horizontal fault plane constrained from seismologic and geodetic observations. *Geophysical Research Letters*, 33(22). https://doi.org/10.1029/2006GL027710

Poli, P., & Prieto, G. A., 2016. Global rupture parameters for deep and intermediate-depth earthquakes. *Journal of Geophysical Research: Solid Earth*, 121(12), 8871-8887. https://doi.org/10.1002/2016JB013521

Potin, B., 2016. *Les Alpes occidentales: tomographie, localisation de séismes et topographie du Moho*, Doctoral dissertation, Université Grenoble Alpes, Grenoble, France.

Ranero, C. R., Villaseñor, A., Phipps Morgan, J., & Weinrebe, W., 2005. Relationship between bend-faulting at trenches and intermediate-depth seismicity. *Geochemistry, Geophysics, Geosystems*, 6(12). https://doi.org/10.1029/2005GC000997

Richards, F. D., Hoggard, M. J., Cowton, L. R., & White, N. J., 2018. Reassessing the thermal structure of oceanic lithosphere with revised global inventories of basement depths and heat flow measurements. *Journal of Geophysical Research: Solid Earth*, 123(10), 9136-9161. https://doi.org/10.1029/2018JB015998

612 Rietbrock, A., & Waldhauser, F., 2004. A narrowly spaced double-seismic zone in the subducting Nazca plate. *Geophysical Research Letters*, 31(10). https://doi.org/10.1029/2004GL019610

614 Ruiz, J. A., & Contreras-Reyes, E., 2015. Outer rise seismicity boosted by the Maule 2010 Mw 8.8 megathrust earthquake. *Tectonophysics*, 653, 127-139. https://doi.org/10.1016/j.tecto.2015.04.007

617 Ruiz, S., & Madariaga, R., 2011. Determination of the friction law parameters of the Mw 6.7 Michilla earthquake in northern Chile by dynamic inversion. *Geophysical Research Letters*, 38(9). https://doi.org/10.1029/2011GL047147

620 Ruiz, S., Tavera, H., Poli, P., Herrera, C., Flores, C., Rivera, E., & Madariaga, R., 2017. The deep Peru 2015 doublet earthquakes. *Earth and Planetary Science Letters*, 478, 102-109. https://doi.org/10.1016/j.epsl.2017.08.036

623 Ruiz, S., Ammirati, J. B., Leyton, F., Cabrera, L., Potin, B., & Madariaga, R., 2019. The January 2019 (Mw 6.7) Coquimbo earthquake: insights from a seismic sequence within the Nazca plate. *Seismological Research Letters*, 90(5), 1836-1843. https://doi.org/10.1785/0220190079

626 Rüpke, L. H., Morgan, J. P., Hort, M., & Connolly, J. A., 2004. Serpentine and the subduction zone water cycle. *Earth and Planetary Science Letters*, 223(1-2), 17-34. https://doi.org/10.1016/j.epsl.2004.04.018

629 Ruppert, N. A., Nayak, A., Thurber, C., & Richards, C., 2020. Aftershock analysis of the 2018 M w 7.1 Anchorage, Alaska, earthquake: Relocations and regional moment tensors. *Seismological Research Letters*, 91(1), 114-125. https://doi.org/10.1785/0220190199

Sambridge, M., 1999. Geophysical inversion with a neighbourhood algorithm—I. Searching a parameter space. *Geophysical Journal International*, 138(2), 479-494. https://doi.org/10.1046/j.1365-246X.1999.00876.x

Scambelluri, M., Pennacchioni, G., Gilio, M., Bestmann, M., Plümper, O., & Nestola, F., 2017. Fossil intermediate-depth earthquakes in subducting slabs linked to differential stress release. *Nature Geoscience*, 10(12), 960-966. https://doi.org/10.1038/s41561-017-0010-7

Sippl, C., Schurr, B., Asch, G., & Kummerow, J., 2018. Seismicity structure of the northern Chile forearc from > 100,000 double-difference relocated hypocenters. *Journal of Geophysical Research: Solid Earth*, 123(5), 4063-4087. https://doi.org/10.1002/2017JB015384

Tassara, A., & Echaurren, A., 2012. Anatomy of the Andean subduction zone: three-dimensional density model upgraded and compared against global-scale models. *Geophysical Journal International*, 189(1), 161-168. https://doi.org/10.1111/j.1365-246X.2012.05397.x

Ulmer, P., & Trommsdorff, V., 1995. Serpentine stability to mantle depths and subduction-related magmatism. *Science*, 268(5212), 858-861. https://doi.org/10.1126/science.268.5212.858

Wang, K., He, J., Schulzeck, F., Hyndman, R. D., & Riedel, M., 2015. Thermal condition of the 27 October 2012 Mw 7.8 Haida Gwaii subduction earthquake at the obliquely convergent queen charlotte margin. *Bulletin of the Seismological Society of America*, 105(2B), 1290-1300. https://doi.org/10.1785/0120140183

Wei, S. S., Wiens, D. A., van Keken, P. E., & Cai, C., 2017. Slab temperature controls on the Tonga double seismic zone and slab mantle dehydration. *Science advances*, 3(1), e1601755. https://doi.org/10.1126/sciadv.1601755

653 Wells, D. L., & Coppersmith, K. J., 1994. New empirical relationships among magnitude, rupture length, rupture width, rupture area, and surface displacement. *Bulletin of the seismological Society of America*, 84(4), 974-1002. https://doi.org/10.1785/BSSA0840040974

656 Wessel, P., Smith, W. H., Scharroo, R., Luis, J., & Wobbe, F., 2013. Generic mapping tools: improved version released. *Eos, Transactions, American Geophysical Union*, 94(45), 409-410. https://doi.org/10.1002/2013EO450001

659 Yuan, X., Sobolev, S. V., Kind, R., Oncken, O., Bock, G., Asch, G., Schurr, B., Graeber, F., Rudloff, A., Hanka, W., Wylegalla, K., Tibi, R., Haberland, Ch., Rietbrock, A., Giese, P., Wigger, P., Röwer, P., Zandt, G., Beck, S., Wallace, T., Pardo, M., & Comte, D., 2000. Subduction and collision processes in the Central Andes constrained by converted seismic phases. *Nature*, 408(6815), 958-961. https://doi.org/10.1038/35050073

Supplementary Material for:

Within the subducting Nazca Plate: The 2020 Mw 6.8 Calama earthquake and its similarity with the surrounding inslab seismicity

Carlos Herrera[1,2], Francisco Pastén-Araya[3,4], Leoncio Cabrera[5], Bertrand Potin[3], Efraín Rivera[4], Sergio Ruiz[3], Raúl Madariaga[3], Eduardo Contreras-Reyes[3]

[1] School of Earth and Ocean Sciences, University of Victoria, Victoria, BC, Canada

[2] Now at: Onur Seemann Consulting, Inc., Victoria, BC, Canada

[3] Departamento de Geofísica, Facultad de Ciencias Físicas y Matemáticas, Universidad de Chile, Santiago, Chile

[4] Departamento de Obras Civiles, Facultad de Ciencias de la Ingeniería, Universidad Católica del Maule, Talca, Chile

[5] ISTerre Institut des Sciences de la Terre, CNRS, Université Grenoble Alpes, Grenoble, France

Contents of this file:

Datasets

Dataset S1: The file SM_1.txt contains the catalog of earthquakes reported by the CSN that were used as templates for template matching. Columns correspond to the date (YYYY-MM-DDThh:mm:ss), latitude (°), longitude (°), depth (km), and magnitude reported on the CSN website: www.sismologia.cl (last accessed on January 21, 2022).

Dataset S2: The file SM_2.txt contains the resulting catalog of earthquakes after running template matching. Columns correspond to the date (YYYY-MM-DDThh:mm:ss), latitude (°), longitude (°), depth (km), and magnitude.

Text S1: Strong motion analysis

The processing of the acceleration waveforms included the removal of the instrument response, mean, and linear trend. Then, a fourth-order Butterworth bandpass filter between 0.1 and 35 Hz was applied. The peak ground acceleration (PGA) at each station was calculated from the geometric average of the maximum accelerations of the two horizontal components. Station AF01 (the closest to the epicenter) recorded the highest PGA of this event, which reached 0.13 g. Ground motion intensities decrease with increasing distance from the earthquake (Figure S3a). Additionally, we calculated spectral accelerations as a function of period (SA(T)) using the geometric average of the 5% damped response spectrum (Nigam & Jennings 1969) of the two horizontal components. PGA and SA(T) observations were compared with the predictions for inslab earthquakes of two recent ground motion models (GMM) developed with Chilean data (Idini *et al*. 2017; Montalva *et al*. 2017). The site parameter required by both GMMs is V_{S30}, which was obtained from the site database compiled by Herrera *et al*. (2020).

Normalized total residuals $Z_t^j(T)$ were calculated for each station j:

$$Z_t^j(T) = \frac{\log_e[I_{obs}^j(T)] - \log_e[I_{pred}^j(T)]}{\sigma(T)}$$

where $I_{obs}^j(T)$ and $I_{pred}^j(T)$ are the observed and predicted ground motion intensities at station j for period T, respectively, and $\sigma(T)$ is the total standard deviation of the GMM for period T, usually provided in log_e units. Residual results are shown in Figure S3b, where in general both GMMs perform well when predicting ground motion intensities at the selected periods, especially at distances within their calibration range, as shown by the nearly zero residuals. As expected, slightly larger residuals are observed at distances greater than this limit, but no systematic deviation from the zero trend as a function of distance is shown by any residual distribution.

Figures

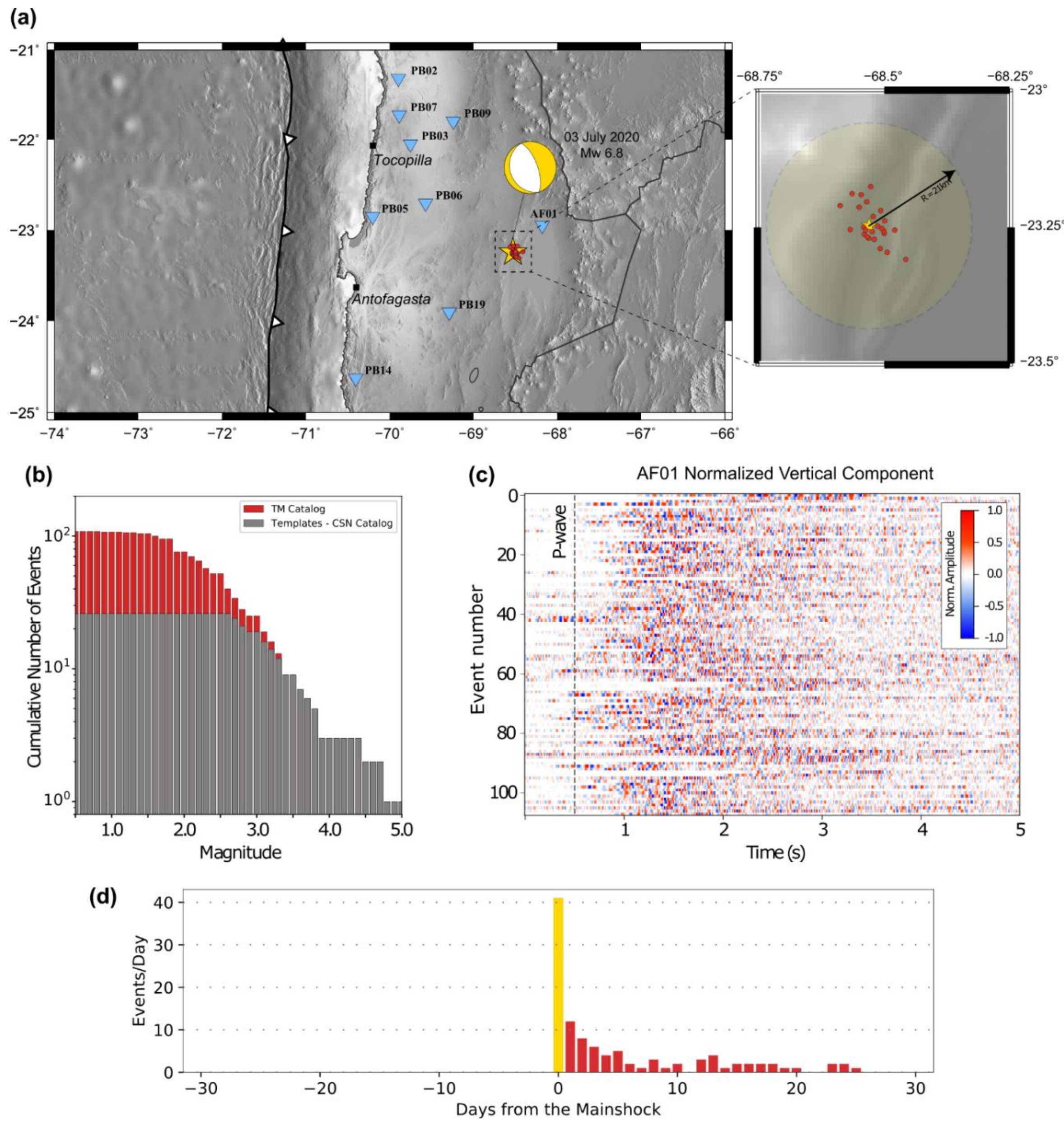

Figure S1: Template matching analysis to detect earthquakes of the Calama seismic sequence. (a) Map showing the broadband stations used, the Calama earthquake with its GCMT focal mechanism, and the aftershocks reported by the CSN (red dots). (b) Frequency-magnitude diagram of the original CSN catalog and the new catalog with events detected through template matching (TM). (c) Normalized waveforms of the new catalog for the vertical component of station AF01, aligned 0.5 s before the estimated P-wave arrival (grey dashed line). Events are sorted based on their occurrence time. (d) Daily number of events before and after then mainshock.

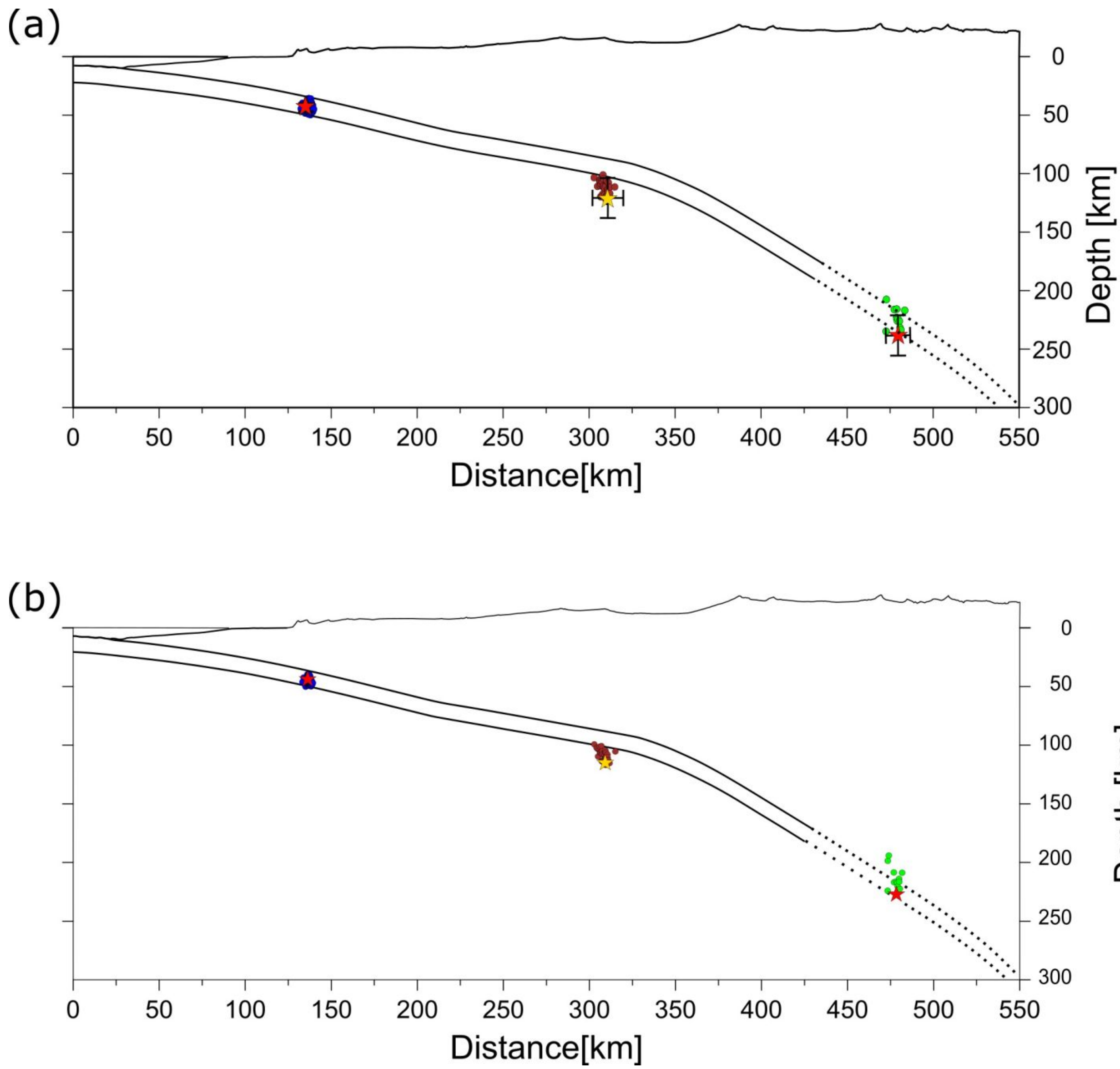

Figure S2: Locations of the three earthquake sequences. Mainshock locations are shown with stars and aftershocks with colored circles. Upper and lower boundaries of the oceanic crust are also shown, which are less resolved at greater depths (segmented lines). (a) Absolute locations. Error bars are also shown for the mainshocks. (b) Relocations obtained with a double difference method.

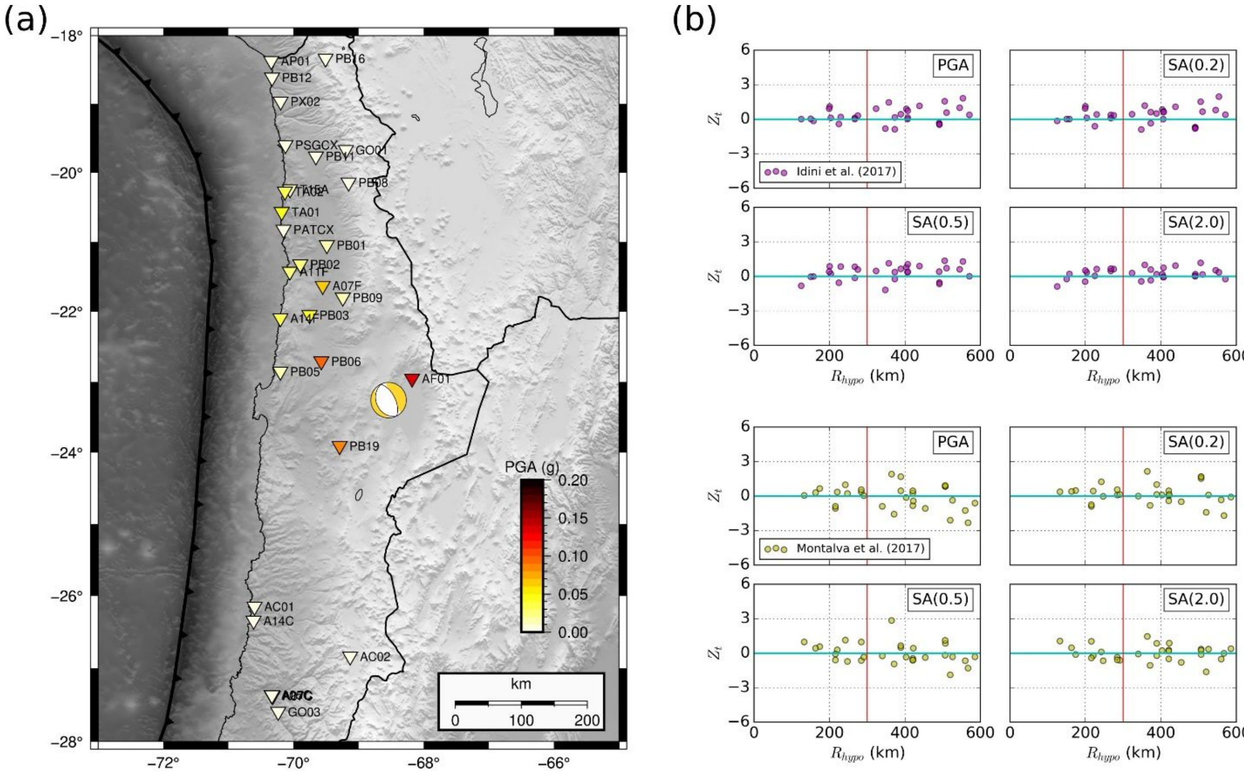

Figure S3: Strong motion analysis of the Calama earthquake. (a) Spatial distribution of the observed PGA at the analyzed stations. The earthquake moment tensor was obtained from GCMT and is located at the epicenter. The trench line was obtained from Bird (2003). (b) Z_t residuals for PGA and SA(T) at three different periods, which are shown in different colors for each GMM. Hypocentral distance (R_{hypo}) is used by both GMMs for inslab earthquakes. The maximum calibration distance of the GMMs is shown by the red lines.

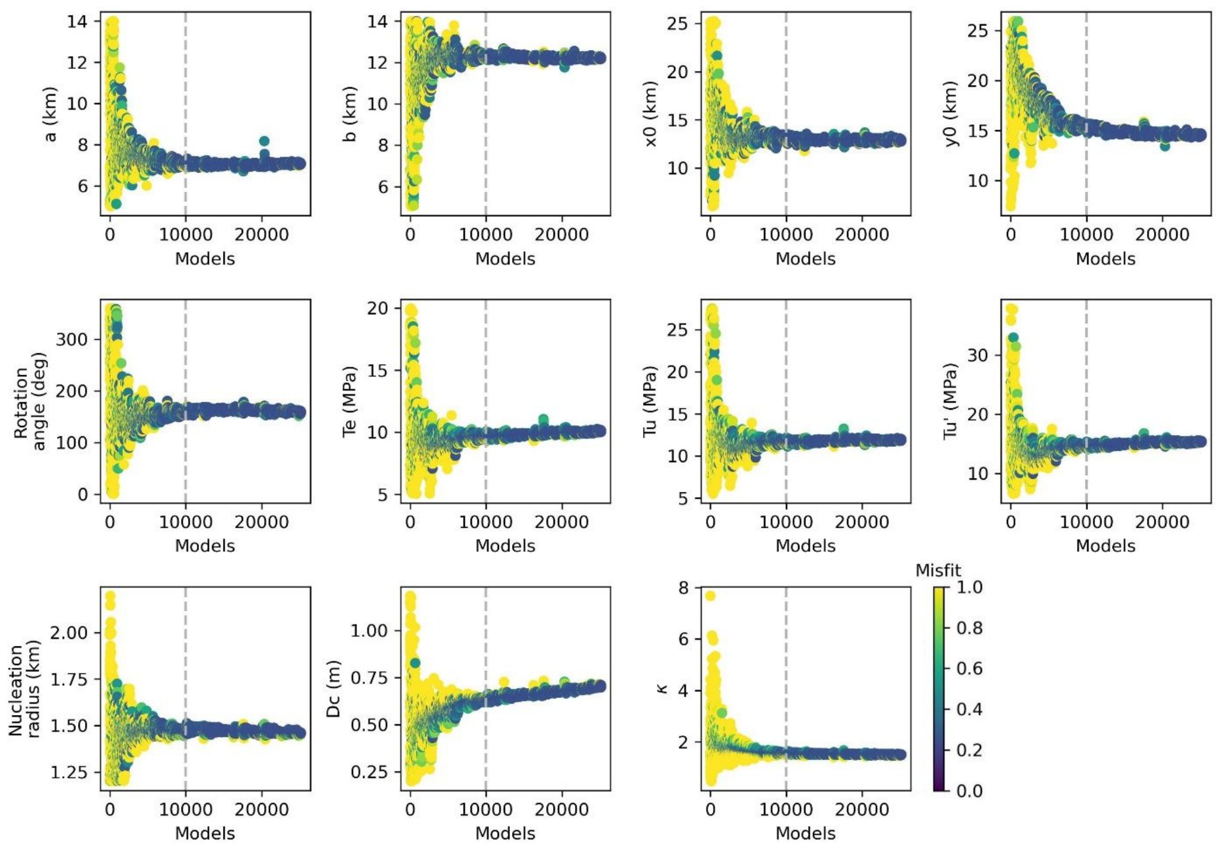

Figure S4: Convergence of the 10 parameters of the dynamic rupture model and κ. All sampled models are shown by dots colored according to their misfit. The gray dashed line in each plot defines the start of the range where model parameters start to converge.

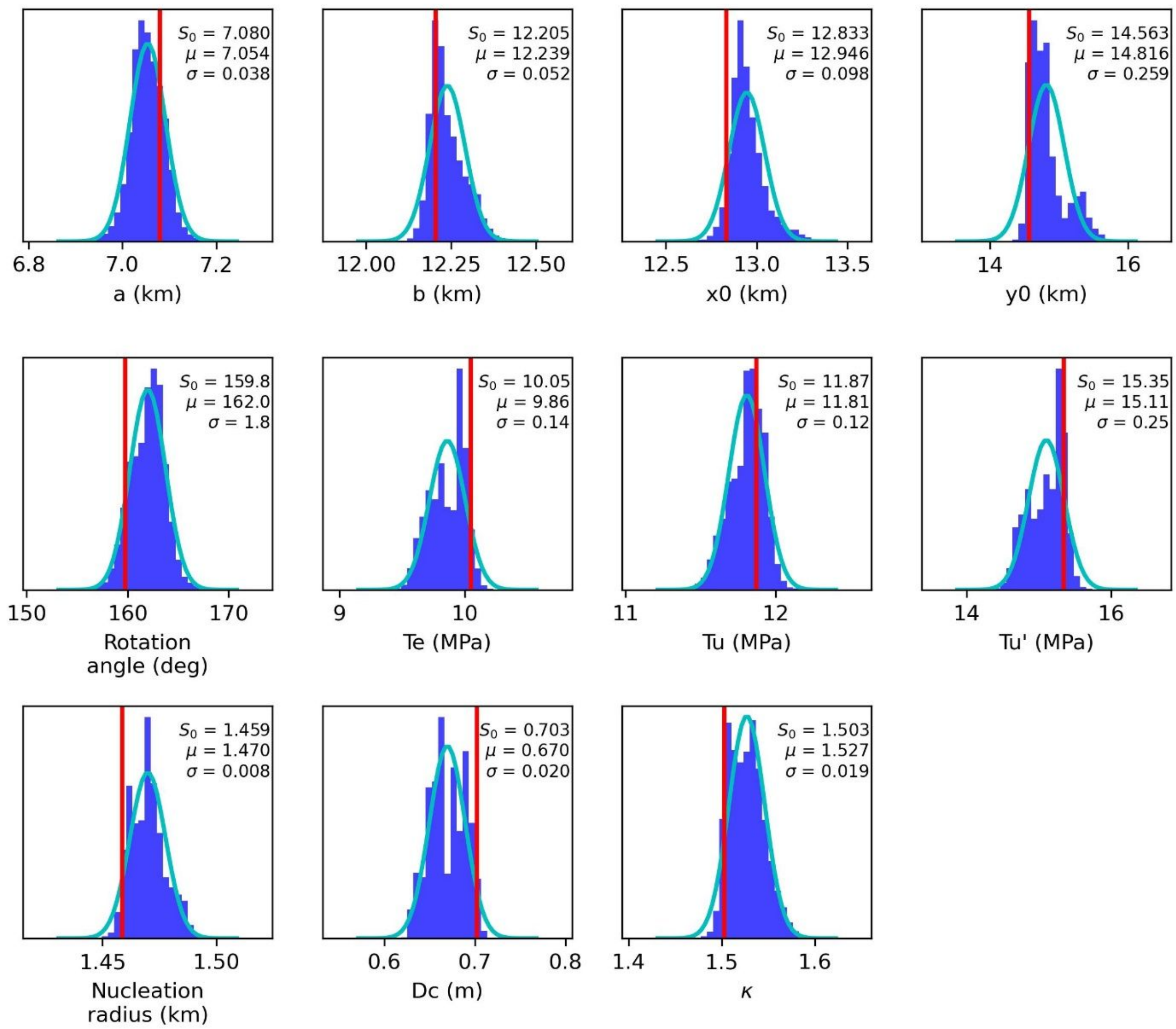

Figure S5: Histograms of the 10 parameters of the dynamic rupture model and κ, calculated within the range where model parameters start to converge (as defined in Figure S2). Cyan curves show the best-fitting Gaussian distributions of mean μ and standard deviation σ. The values of the best model (S_0) are shown with red lines.

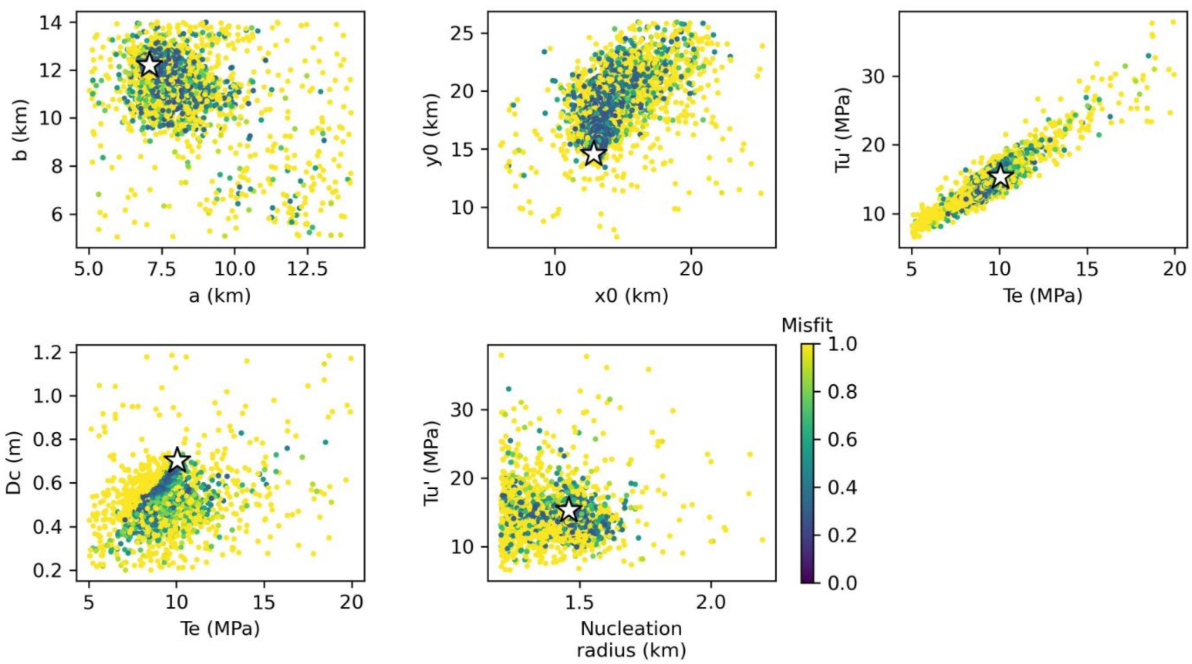

Figure S6: 2-D distribution between parameters of the dynamic rupture model. All sampled models are shown by dots colored according to their misfit. The white star in each plot shows the values associated to the best model.

References

Bird, P., 2003. An updated digital model of plate boundaries. *Geochemistry, Geophysics, Geosystems*, 4(3). https://doi.org/10.1029/2001GC000252

Herrera, C., Cassidy, J. F., Dosso, S. E., Bastías, N., & Onur, T., 2020. Ground-Motion Evaluation of Moderate and Large Interface Earthquakes along the Chilean Subduction Zone. *Bulletin of the Seismological Society of America*, 110(6), 2693-2710. https://doi.org/10.1785/0120190265

Idini, B., Rojas, F., Ruiz, S., & Pastén, C., 2017. Ground motion prediction equations for the Chilean subduction zone. *Bulletin of Earthquake Engineering*, 15(5), 1853-1880. http://dx.doi.org/10.1007/s10518-016-0050-1

Montalva, G. A., Bastías, N., & Rodriguez-Marek, A., 2017. Ground-Motion Prediction Equation for the Chilean subduction zone. *Bulletin of the Seismological Society of America*, 107(2), 901-911. https://doi.org/10.1785/0120160221

Nigam, N. C., & Jennings, P. C., 1969. Calculation of response spectra from strong-motion earthquake records. *Bulletin of the Seismological Society of America*, 59(2), 909-922. https://doi.org/10.1785/BSSA0590020909